MATERIALS CHEMISTRY FRONTIERS

CCS 中国化学会 CHINESE CHEMICAL SOCIETY

ICCAS

ROYAL SOCIETY OF CHEMISTRY

A combined experimental and computational approach reveals how aromatic peptide amphiphiles self-assemble to form ion-conducting nanohelices

Journal:	*Materials Chemistry Frontiers*
Manuscript ID	QM-RES-06-2020-000369.R1
Article Type:	Research Article
Date Submitted by the Author:	22-Jul-2020
Complete List of Authors:	Wang, Yin; Virginia Tech, Chemistry An, Yaxin; Virginia Tech, Department of Chemical Engineering Shmidov, Yulia; Ben-Gurion University of the Negev, Chemical Engineering Bitton, Ronit; Ben-Gurion University of the Negev, Deshmukh, Sanket; Virginia Tech, Chemical Engineering Matson, John; Virginia Tech, Chemistry

A combined experimental and computational approach reveals how aromatic peptide amphiphiles self-assemble to form ion-conducting nanohelices

Yin Wang[1,#], Yaxin An[2,#] ,Yulia Shmidov[3], Ronit Bitton[3], Sanket A. Deshmukh[2,*], John B. Matson[1,*]

[1] Department of Chemistry, Virginia Tech Center for Drug Discovery, and Macromolecules Innovation Institute, Virginia Tech, Blacksburg, VA 24061, United States. Email: jbmatson@vt.edu

[2] Department of Chemical Engineering, Virginia Tech, Blacksburg, VA 24061, United States. Email: sanketad@vt.edu

[3] Department of Chemical Engineering and the Ilse Katz Institute for Nanoscale Science and Technology, Ben-Gurion University of the Negev, Beer-Sheva 84105, Israel

[#] These authors contributed equally to this work.

Abstract

Reported here is a combined experimental-computational strategy to determine structure-property-function relationships in persistent nanohelices formed by a set of aromatic peptide amphiphile (APA) tetramers with the general structure $\mathbf{K_SXEK_S}$, where K_S= *S*-aroylthiooxime modified lysine, X = glutamic acid or citrulline, and E = glutamic acid. In low phosphate buffer concentrations, the APAs self-assembled into flat nanoribbons, but in high phosphate buffer concentrations they formed nanohelices with regular twisting pitches ranging from 9–31 nm. Coarse-grained molecular dynamics simulations mimicking low and high salt concentrations matched experimental observations, and analysis of simulations revealed that increasing

strength of hydrophobic interactions under high salt conditions compared with low salt conditions drove intramolecular collapse of the APAs, leading to nanohelix formation. Analysis of the radial distribution functions in the final self-assembled structures led to several insights. For example, comparing distances between water beads and beads representing hydrolysable K_S units in the APAs indicated that the K_S units in the nanohelices should undergo hydrolysis faster than those in the nanoribbons; experimental results verified this hypothesis. Simulation results also suggested that these nanohelices might display high ionic conductivity due to closer packing of carboxylate beads in the nanohelices than in the nanoribbons. Experimental results showed no conductivity increase over baseline buffer values for unassembled APAs, a slight increase (0.4×10^2 μS/cm) for self-assembled APAs under low salt conditions in their nanoribbon form, and a dramatic increase (8.6×10^2 μS/cm) under high salt conditions in their nanohelix form. Remarkably, under the same salt conditions, these self-assembled nanohelices conducted ions 5–10-fold more efficiently than several charged polymers, including alginate and DNA. These results highlight how experiments and simulations can be combined to provide insight into how molecular design affects self-assembly pathways; additionally, this work highlights how this approach can lead to discovery of unexpected properties of self-assembled nanostructures.

Introduction

Complex self-assembly processes occur in natural and synthetic systems to form functional nanostructured materials; well-known examples include the supramolecular polymerization of tubulin to form microtubules that give cells their shape[1, 2] and the non-covalent association of synthetic peptide amphiphiles into various one-dimensional nanostructures that can entangle to form hydrogels.[3-7] In an effort to determine structure-property-function relationships in self-assembled materials, researchers seek to understand how specific nanostructures form from certain building blocks, with the ultimate goal of controlling the shape, nanoscale dimensions, and resultant applications of self-assembled materials through rational molecular design.[8-10] Often some knowledge of how molecular design influences the ultimate self-assembled structure can be determined experimentally, for example by using TEM to measure nanostructure dimensions or molecular level techniques such as IR spectroscopy to determine

how hydrogen bonds align. Furthermore, how the self-assembled structure affects the potential applications can be probed experimentally as well,[11, 12] for instance, by applying impedance spectroscopy to evaluate the conductivity of peptide fibers.[13, 14] However, even the combination of several experimental techniques only provides limited information on self-assembled structures, pathways, and properties. Fortunately, simulations that accurately reproduce experimental results can often fill in the gaps, revealing details that experiments cannot by enabling direct visualization of self-assembly processes over time.[15, 16] Therefore, combined experimental-computational approaches, with results from each feeding the other, can reveal new insights into how molecular design influences structure and function in self-assembled materials. In some cases, combined studies may even suggest new phenomena that might be overlooked using experiments or computations alone.[17]

We recently reported on a self-assembling aromatic peptide amphiphile (APAs) that forms persistent and regular helical nanostructures (Fig. 1) with the structure $\mathbf{K_SEEK_S}$, where K_S= *S*-aroylthiooxime modified lysine and E = glutamic acid.[18] Surprisingly, we found that these nanostructures were very stable, in contrast with most other reported self-assembled nanohelices, which lie on a self-assembly pathway between nanoribbons and nanotubes[19-23] and need chemical crosslinking to stabilize the helical structure.[24, 25] Notably, a similar APA formed nanohelices that were even stable enough to grow silver nanoparticles (AgNPs) on them to make helical arrays of AgNPs.[26] However, the self-assembly process through which these nanohelices form, the intermolecular forces leading to nanohelix formation, and the

question of why these APA nanohelices do not collapse to form nanotubes remained unknown. Therefore, we set out to address these questions by exploring and expanding on this class of APAs using a combined experimental/computational approach, with the goals of answering these questions and providing more general insight into how to design self-assembled helical nanostructures.

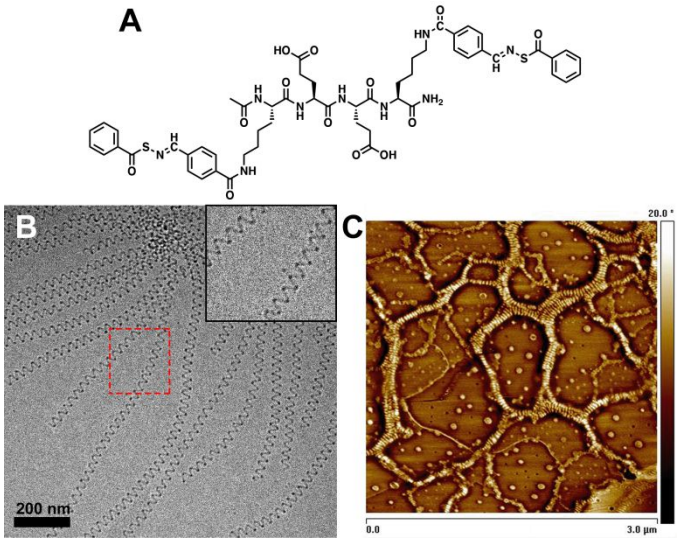

Fig. 1 (A) Molecular structure of APA $\mathbf{K_SEEK_S}$. (B) Cryo-TEM and (C) AFM phase images of nanohelices formed by $\mathbf{K_SEEK_S}$ in 10 mM phosphate buffer at the concentration of 1 mM. Inset in the top right corner of panel B shows the zoomed-in image of the area outlined by the dashed red rectangle. Reproduced with permission from reference 18.

Specifically, we aimed to understand the self-assembly process for APAs with the general structure $\mathbf{K_SXEK_S}$ (X = variable amino acid residue) with the goals of understanding which forces lead to formation of nanohelices (rather than other nanostructures), how the molecular shape of the APAs influences helix formation, and what amino acids are required for self-assembly into nanohelices. In terms of experimental parameters, we envisioned that we could

vary salt concentration to change the degree of charge screening in the carboxylate residues, and vary the amino acid in the X position to tune the shape of the molecules and learn which amino acids are key for helix formation. We also envisioned that coarse-grained (CG) molecular dynamics (MD) simulations could complement experiments. For example, by varying interaction parameters between beads as well as the type of beads, we could mimic changes in salt concentration or amino acid sequence, respectively, and visualize how changing these parameters would affect nanostructures. Analysis of the nanostructures formed in the MD simulations would confirm that our MD models matched experimental results and then allow us to determine what interactions were critical for nanohelix formation. Finally, we aimed to allow the MD simulations to direct additional experiments that would both confirm their structural accuracy and point toward new applications. Overall, we describe here how our integrated experimental/computational approach revealed how supramolecular interactions can be tuned to generate persistent helical nanostructures, and we detail how these studies led to our discovery of unexpected ion conductivity properties in these APAs.

Results and discussions

Molecular Design

We began by synthesizing two APAs that contained *S*-aroylthiooximes (SATOs),[27] an aromatic unit developed in our lab that drives self-assembly in APAs.[18, 28-30] Specifically, *S*-benzoylthiohydroxylamine (SBTHA) was added in a condensation reaction, affording two different APAs with the general structure $\mathbf{K_SXEK_S}$: $\mathbf{K_SNEK_S}$ and $\mathbf{K_S}\boldsymbol{C'}\mathbf{EK_S}$ (Fig. 2G). We

chose asparagine (N) and citrulline (*C'*) as the variable residues because their amide and urea groups, respectively, offer the potential for additional hydrogen bonding beyond the backbone amide groups. Two control APAs that included an oxime in place of the SATO linkage were also prepared ($\mathbf{K_ONEK_O}$ and $\mathbf{K_O}\boldsymbol{C'}\mathbf{EK_O}$, where K_O represents an oxime-functionalized lysine residue), replacing SBTHA with *O*-benzylhydroxylamine. Detailed synthetic procedures and characterization can be found in the Supporting Information (Figs. S1 and S2).

Molecular Self-Assembly and Salt-induced Morphological Transition

Cryogenic transmission electron microscopy (cryo-TEM) (Fig. 2A−D) and conventional TEM imaging (Fig. S3) revealed that both APAs assembled into one-dimensional nanostructures in aqueous solution. In 10 mM phosphate buffer (PB), both $\mathbf{K_SNEK_S}$ and $\mathbf{K_S}\boldsymbol{C'}\mathbf{EK_S}$ assembled into nanoribbons, with widths of 6 ± 1 nm and irregularly spaced twists at long intervals (Figs. 2A, 2B, S3A, and S3C). In both cases, the thickness of these twisted nanoribbons was around 5 nm, which is equal to the expected thickness of a partially or fully interdigitated bilayer, implying that the observed nanoribbons were likely bilayer structures generated by association of the aromatic SATO surfaces. This type of bilayer molecular packing behavior is widely found in peptide systems composed of uniform $(AB)_n$ amino acid periodicity (where A and B are polar and nonpolar residues, respectively).[6, 13, 31-33]

Because $\mathbf{K_SNEK_S}$ and $\mathbf{K_S}\boldsymbol{C'}\mathbf{EK_S}$ assembled into nanoribbons, we originally concluded that only $\mathbf{K_SEEK_S}$, studied previously, was capable of self-assembling into nanohelices. However,

given their similar chemical structures to the nanohelix-forming APAs, we expected that **K_SNEK$_S$** and **K_S*C'*EK$_S$** might form nanohelices under specific conditions. Thus, we were inspired to investigate self-assembly in solutions with variable PB concentrations based on work from others on salt-induced morphological changes in self-assembled peptides.[34-36] In general, addition of salts can facilitate peptide self-assembly because salts can screen charges in peptides with acidic or basic residues, weakening repulsive forces and promoting molecular packing. For example, Castelletto and coworkers showed that increasing salt concentration induced a morphology change from twisted nanofibers to nanotubes in a specific heptapeptide.[34] Encouraged by these and related reports,[35, 37, 38] we investigated how the self-assembled morphology changed at different PB concentrations.

When the concentration of PB was increased from 10 mM to 100 mM, dramatically different self-assembled morphologies were observed for the APAs. Specifically, **K_SNEK$_S$** assembled into tight nanohelices (similar to a telephone cord) along with twisted nanoribbons at 100 mM PB (Figs. 2C and S3B). The pitch for **K_SNEK$_S$** nanohelices was 13 ± 2 nm which is much tighter than that of **K_SEEK$_S$** nanohelices (32 ± 4 nm) found in our recent report.[18] We attribute the formation of these tight nanohelices to the uncharged nature of the N residue in **K_SNEK$_S$**, which has one fewer charged amino acid residue than **K_SEEK$_S$**, leading to reduced repulsion between individual APAs and tighter molecular packing under high salt conditions. In contrast, APA **K_S*C'*EK$_S$** assembled into only helical nanostructures in 100 mM PB, as a mixture of both loose and tight nanohelices (Figs. 2D and S3D). The pitch of the loose nanohelices was 31 ± 2

nm, and that of the tight ones was 9 ± 1 nm; each had diameters of ~6 nm. Given that the diameter of nanohelices formed at 100 mM PB was identical to those at 10 mM PB, it can be inferred that the nanohelices of $\mathbf{K_SNEK_S}$ and $\mathbf{K_S}\boldsymbol{C'}\mathbf{EK_S}$ evolved from nanoribbons because of charge screening effects provided by buffer salts, decreasing the repulsive force among the APAs. Remarkably, although there are two types of morphologies for both APAs in high PB concentration, they were kinetically stable; for example, no significant difference in morphology was observed for $\mathbf{K_S}\boldsymbol{C'}\mathbf{EK_S}$ even after incubation in 100 mM PB for 14 d at rt (Fig. S8). To the best of our knowledge, this is the first reported observation of nanohelix formation triggered by an increase in salt concentration. Interestingly, nanoribbons rather than nanohelices were found for both control APAs ($\mathbf{K_ONEK_O}$, $\mathbf{K_O}\boldsymbol{C'}\mathbf{EK_O}$) in both 10 mM and 100 mM PB (Fig. S4), which indicates that the SATO group is critical, at least in these APAs, for driving nanohelix morphology.

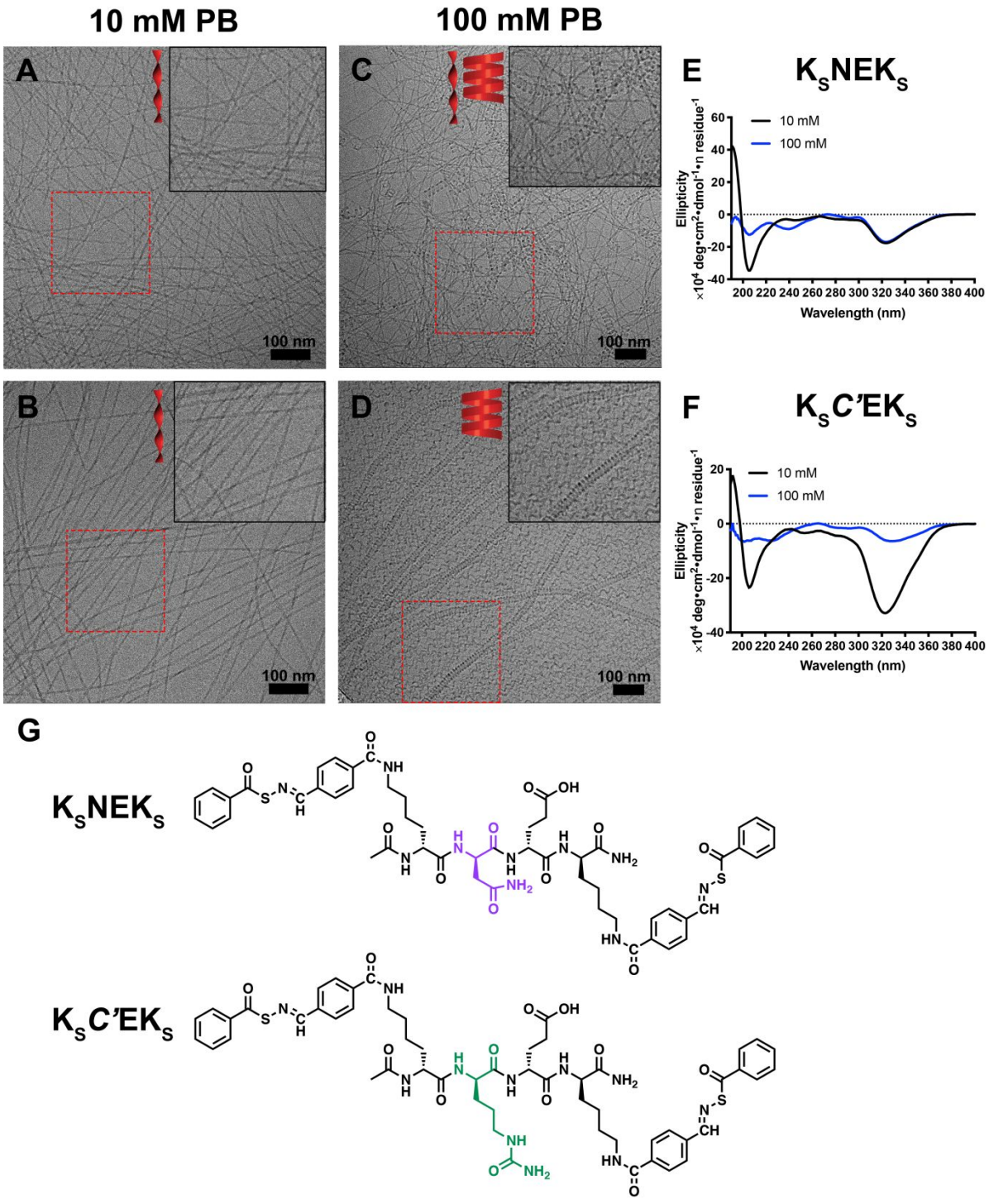

Fig. 2 (A-D) Cryo-TEM characterization in aqueous solution illustrates the effect of salt concentration on the self-assembled morphology of both APAs. In 10 mM PB: (A) Cryo-TEM image of twisted nanoribbons formed by $\mathbf{K_SNEK_S}$; (B) Cryo-TEM image of twisted nanoribbons formed by $\mathbf{K_SC'EK_S}$. In 100 mM PB: (C) Cryo-TEM image of nanohelices and

twisted nanoribbons formed by **K_SNEK_S**; (D) Cryo-TEM image of nanohelices formed by **K_S*C'*EK_S**. Insets in the top right corners of panels A-D show zoomed-in images of the areas outlined by the dashed red rectangles. Solution concentration: 1 mM APAs in phosphate buffer (pH 7.4). Circular dichroism (CD) spectra of (E) **K_SNEK_S** and (F) **K_S*C'*EK_S** in 10 mM or 100 mM phosphate buffer (pH 7.4) at a concentration of 100 μM. (G) Molecular structures of both APAs studied in the present work. Residues asparagine (N) and citrulline (*C'*) are highlighted in color.

Effect of Salt Concentration on Molecular Packing

To understand the assembly differences between these two APAs, we conducted Nile Red assays to evaluate their critical aggregation concentrations (CACs), along with circular dichroism (CD), and Fourier-transform infrared (FTIR) spectroscopy measurements to study the molecular packing of the self-assembled APAs. The Nile Red assay showed that the CAC value for both APAs was in the range of 30 μM in 10 mM PB (Fig. S5 and Table S1). This is consistent with previous CAC measurements on similar APAs.[18, 29, 39, 40] CD spectroscopy revealed that the secondary structures of these peptide nanoassemblies were similar, and both displayed strong signals in the peptide region (190−240 nm) and in the SATO characteristic absorption region (300−360 nm), consistent with SATO absorptions in the corresponding UV−vis spectra (Fig. S6). In 10 mM PB, both **K_SNEK_S** and **K_S*C'*EK_S** showed spectra consistent with a mixture of random coil and β-sheet secondary structures (black curves, Figs. 2E and 2F). The spectra for both APAs changed significantly as the salt concentration increased

from 10 mM to 100 mM (blue curves, Figs. 2E and 2F), consistent with their morphological changes. The absorption peak in the SATO region for **K_SNEK_S** remained nearly identical at the different PB concentrations, but it decreased greatly in intensity for **K_S*C'*EK_S**. As SATOs also have absorptions in the 190–240 nm region, definitive interpretations of the CD data are difficult; however, the spectral differences observed in the APAs upon increasing the salt concentration indicates that the molecular packing within the nanoassemblies changed in response to salt addition. Regardless of salt concentration, both APAs exhibited amide I peaks located near 1630 cm^{-1} in FTIR spectra (Fig. S7), indicative of β-sheet secondary structures.[29, 41] However, due to the complexity of these APAs, we cannot rule out the possibility that other carbonyl compounds absorb in this range.

To explore how PB buffer concentrations influenced the observed morphological changes from nanoribbons to nanohelices in **K_SNEK_S** and **K_S*C'*EK_S**, we used conventional TEM to monitor the transition. **K_SNEK_S** was chosen as the example APA because it contains a traditional amino acid residue in the X position, making the secondary interactions simpler to model in simulations (see below) than in **K_S*C'*EK_S**. As shown in Fig. 3A, twisted nanoribbons were observed in 10 mM PB, consistent with our observations using cryo-TEM. At 20 mM PB (Fig. 3B), some nanoribbons began to roll up (red arrows), but twisted nanoribbons were still the dominant morphology. Further increasing the salt concentration to 25 mM, tight nanohelices began to appear, as indicated by the bright edges of the helices and the dark middle regions (Fig. 3C). Closer examination of the ends of these tight nanohelices revealed that they resulted

from a transformation of the original nanoribbons shown in Fig. 3A. We base this conclusion on two observations: 1) The diameter of the nanohelices was identical to the width of the nanoribbons; and 2) The ends of these tight nanohelices were flat (red arrows in Fig. 3C). A small number of toroids were also observed under these assembly conditions, possibly as a result of the drying process in conventional TEM considering that they were not observed by cryo-TEM. Further increasing salt concentration to 30 mM induced the generation of more nanohelices and toroids (Fig. 3D). Remarkably, when the salt concentration reached 50 mM or above, almost all the nanoribbons turned into nanohelices (Figs. 3E and 3F). The flat ends of the nanohelices (red arrow in Fig. 3E) confirmed the morphological transition from nanoribbons to nanohelices as the salt concentration increased.

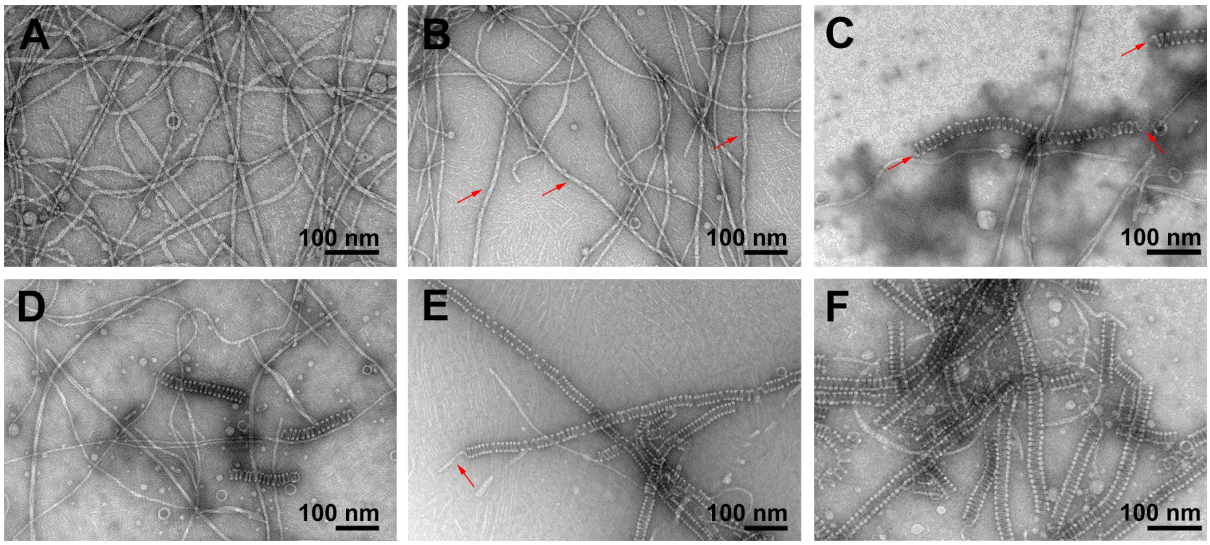

Fig. 3 Conventional TEM characterization of $\mathbf{K_SNEK_S}$ illustrates the salt-induced morphological transition from nanoribbons to nanohelices. All grids were stained with uranyl acetate prior to imaging. APA concentration was 100 μM. PB concentration was (A) 10 mM; (B) 20 mM; (C) 25mM; (D) 30 mM; (E) 50 mM; (F) 100 mM.

Coarse-grained Molecular Dynamics Simulations on Molecular Self-Assembly

To gain more insight into nanohelix formation, we explored the interactions and mechanism involved in nanoribbon and nanohelix formation using coarse-grained (CG) molecular dynamics (MD) simulations.[42-44] Details on the simulation set-up are provided in the Supporting Information. The CG MD simulations allowed us to easily alter the interaction parameters between different types of beads in an effort to probe which interactions are vital for nanoribbon and nanohelix formation, and how changes in these interactions drive the salt-induced conversion from nanoribbon to nanohelix. We envisioned that key interactions would be between QAE beads, which represent the glutamic acid COOH group (this bead was kept neutral in this study), and between SC4F beads, which represent the benzene rings in the SATO units (see Fig. S9 for mapping scheme). We began by using the original MARTINI force-field (FF) parameters for ε[QAE-QAE] and ε[SC4F-SC4F], which are 1.19503 and 0.62739 kcal/mol, respectively (Table S2).[42] These ε values in the 12-6 Lennard-Jones potential depict the strength of interactions between two beads.[45] Under these parameters, concentrations of APAs in simulations were explored first. We found that nanoribbons with bilayer structures formed over the course of 15 μs when the number of APA molecules was 150 in an equilibrated water box with the size of ~ 17 x 17 x 17 nm^3. When the number of APA molecules was decreased (50 or 100 molecules) or increased (300 molecules), micelles and hybrid irregular nanohelix/nanofibers formed, respectively. Therefore, we used 150 APA molecules in all subsequent simulations. Figure S10A shows the snapshot of the structure of the resulting nanoribbon with a thickness of ~4.5 nm and a width of ~15 nm. The final bilayer thickness

measurement was consistent with cryo-TEM observations of $\mathbf{K_SNEK_S}$ at low PB concentration (5 nm), but the simulated nanoribbon width (15 nm) was substantially bigger than that observed by cryo-TEM (6 nm). We attribute this expansion of the ribbon width to interactions between APAs that this model did not perfectly capture. To further probe how ε[SC4F-SC4F] interactions affected the dimensions of the nanoribbons, we gradually increased the ε[SC4F-SC4F] from 0.62739 to 1.0 kcal/mol while keeping the value of ε[QAE-QAE] constant at its original value. At ε[SC4F-SC4F] = 0.8 kcal/mol, a nanoribbon formed with a width of ~7.5 nm and a thickness of ~4.5 nm (Fig. S10B), which was in good agreement with the dimensions of the experimentally observed nanoribbons.

Using these interaction parameters that reproduced the experimentally observed nanoribbon dimensions, we conducted time-course studies to gain molecular-level insights into a possible self-assembly pathway (Fig. 4A). These efforts revealed that $\mathbf{K_SNEK_S}$ APAs first aggregated to form small clusters of ~40 $\mathbf{K_SNEK_S}$ molecules each, with each cluster merging into one U-shaped intermediate at ~0.6 μs. The U-shaped intermediates gradually moved closer to each other until they were connected at ~1.3 μs; they further evolved into a continuous ribbon-like structure with rough edges (bumps) at 3.3 μs. These bumps disappeared as the self-assembly process continued, and a nanoribbon structure finally formed at ~10 μs, which was stable for the remainder of simulation up to ~15 μs. Movies showing the formation of nanoribbons in the above CG MD simulations can be found in the Supporting Information. As expected, hydrophobic beads (e.g., SC4F) were located inside the nanoribbon, while the hydrophilic QAE

(COOH) and P5 ($CONH_2$) beads were at the outer surfaces (Fig. S10B).[46, 47] Because the ε[QAE-QAE] interaction parameter was stronger than ε[SC4F-SC4F] in these simulations, the interactions between hydrophilic QAE beads with themselves and between the hydrophilic QAE beads with water (P4 beads) dominated the self-assembly process (ε[QAE-P4] = 1.3 kcal/mol and ε[SC4F-P4] = 0.6 kcal/mol).

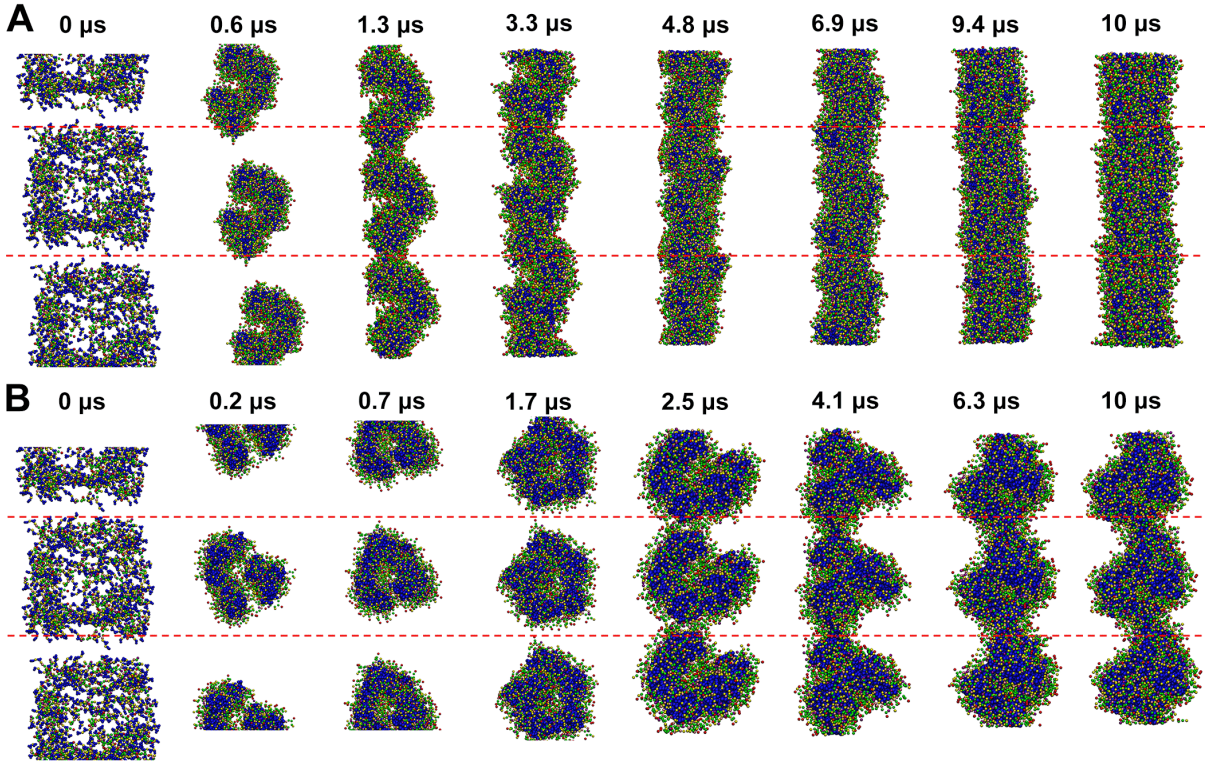

Fig. 4 Self-assembly process of (A) nanoribbon and (B) nanohelix formation by CG MD simulations. Beads for water are not shown for clarity. Red dotted lines represent periodic boundaries. Simulations were performed for 15 μs, and the nanoribbon and nanohelix structures were stable from 10 through 15 μs. Color schemes of beads can be found in Fig. S9. Zoomed-in snapshots for both nanostructures at ~15 μs are shown in Fig. S10.

Experimental and computational studies have shown that screening of charges under high salt conditions causes hydrophobic interactions to dominate the self-assembly process.[48-51] This phenomenon is consistent with our experimental results, where we found that hydrophobic interactions increased when the salt concentration was increased from 10 mM to 100 mM, as indicated by a hypochromic shift in the local absorption maximum of each APA (Fig. S6).[41, 52] In the Lennard-Jones potential, ε values represent the strength of interactions between specific atom/bead pairs in a system, with larger ε values representing stronger the interactions.[53, 54] To mimic this increase in the hydrophobicity of the APAs, we gradually increased ε[SC4F-SC4F] from 0.62739 kcal/mol to 1 kcal/mol and decreased ε[QAE-QAE] from 1.19503 kcal/mol to 0.6 kcal/mol. In this series of simulations, these changes to the interaction parameters resulted in nanohelix formation, with dimensions similar to those observed in experiments. In other words, the CG MD simulations supported our hypothesis that relatively stronger interactions between hydrophobic beads and relatively weaker interactions between hydrophilic beads resulted in the nanohelix structure (Figs. 4B and S10C).[55] Different from the assembly pathway in nanoribbon formation, small, discrete aggregates of ~15 $\mathbf{K_SNEK_S}$ molecules formed at the early stages of the simulation (0–0.15 μs). These small aggregates quickly merged to create larger aggregates of 50–100 $\mathbf{K_SNEK_S}$ molecules at ~0.2 μs and further developed into twisted, fiber-like aggregates. As the twisted fibers moved closer to each other, they connected at ~2.5 μs, further evolving into nanohelices during the final 7.5 μs of the simulations. Movies showing the formation of nanohelices in the above CG MD simulations can be found in the Supporting Information. The diameter of the final nanohelices was ~4.5 nm, and their pitch was ~8 nm,

close to the tight nanohelices measured by cryo-TEM shown in Fig. 2 (6 nm in diameter and a 13 nm pitch).

To validate that the QAE-QAE interactions are critical in determining this nanohelix structure, we performed additional CG MD simulations, in which we decreased the interaction strength between other hydrophilic beads such as P5 in the neighborhood of QAE beads. Details on the scaled parameters can be found in Table S3. We did not observe nanohelix formation in any of these simulations, which further validates the critical role played by QAE-QAE and SC4F-SC4F beads in determining these self-assembled structures. Thus, our simulations clearly suggest that the balance between hydrophilic and hydrophobic interactions is important in driving the self-assembled structures of these APAs.

To further understand the effect of the change in hydrophilic and hydrophobic interactions on the structure of assembled APAs, the end-to-end distance of each $\mathbf{K_SNEK_S}$ molecule was analyzed in both simulations. The strong interactions between the hydrophobic SC4F-SC4F beads led to smaller end-to-end distances in $\mathbf{K_SNEK_S}$ molecules under simulations mimicking high salt conditions (nanohelix formation) than under low salt conditions (nanoribbon formation) (Fig. 5A). For example, the probability of $\mathbf{K_SNEK_S}$ molecules with end-to-end distances from 4–12 Å was higher in nanohelices than in nanoribbons (42% vs. 31%). Representative CG $\mathbf{K_SNEK_S}$ models with different end-to-end distances are shown in Fig. 5D.

We also analyzed the radial distribution functions (RDFs) between various bead pairs in both types of simulations (Figs. 5B and S11). In the RDF between SC4F (aromatic groups in the SATO units) and P4 (water) beads in Fig. 5B, the first peak was observed at 5 Å, which suggests that P4 beads accumulate around SC4F beads at a distance of 5 Å, forming a hydration shell. The higher peak in the nanohelices RDF indicates that SCF4 beads are on average more hydrated in nanohelices than in nanoribbons. We attribute the higher hydration of the nanohelices compared with the nanoribbons to their helical nature, allowing for water to more easily access the nanohelix core. One possible explanation is that the helical nature of the nanohelices may expose more surface area of SATO units to water compared to nanoribbons. We carried out solvent accessible surface area (SASA) calculations, which suggest that the SASA for nanohelices is higher than that of nanoribbons (1250 ± 80 nm^2 versus 1140 ± 30 nm^2).

Investigations into Molecular Hydrolysis and Ion-conductivity Guided by CG MD Simulations

To test whether the SATO groups in the nanohelices were in fact more hydrated than those in the nanoribbons, we performed a hydrolysis experiment. SATO groups hydrolyze slowly in water,[56] and we expected that if the RDF data derived from the simulations was correct, then hydrolysis of $\mathbf{K_SNEK_S}$ should be faster in 100 mM PB than in 10 mM PB (both pH 7.4). Using UV-vis to follow SATO hydrolysis, we found that $\mathbf{K_SNEK_S}$ (1 mM) hydrolyzed nearly twice as fast in 100 mM PB than in 10 mM PB (Fig. S12). This experimental result supports our

conclusion from the RDFs derived from the simulations, indicating that the cores of the nanohelices are more hydrated than those of the nanoribbons.

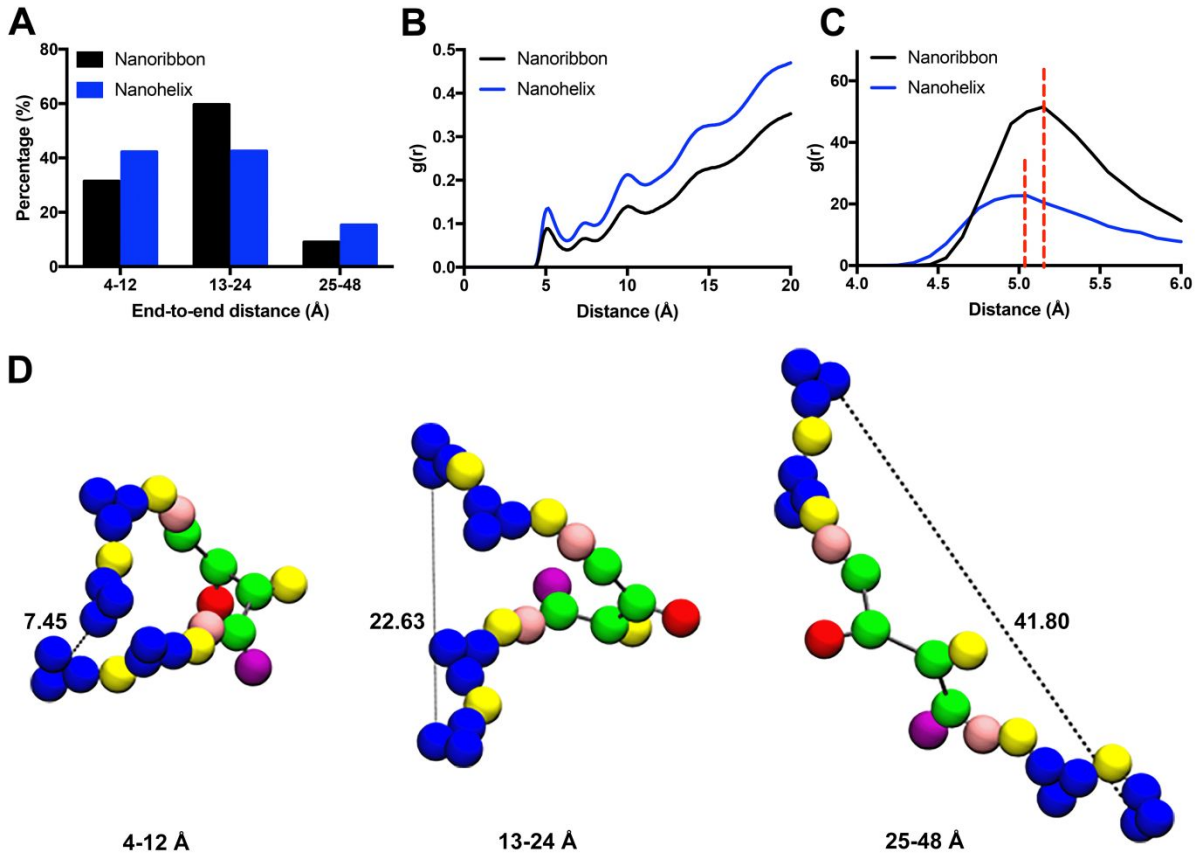

Fig. 5 (A) Probability distributions of end-to-end distance of $\mathbf{K_SNEK_S}$ molecules in nanoribbons and nanohelices with three bins in the range from 4 to 48 Å. (B) Radial distribution function between SC4F beads (aromatic groups) and P4 beads (water). (C) Radial distribution function between QAE and QAE beads (carboxylic acid groups) from 4 Å to 6 Å. (D) Representative structures of $\mathbf{K_SNEK_S}$ molecules with different end-to-end distances; color schemes for beads in panel D can be found in Fig. S9.

We also noticed from RDFs between QAE beads (Fig. 5C), which represent carboxylic acid groups, that these beads were, on average, closer together in the nanohelices than in the

nanoribbons. Because carboxylates can conduct ions, we asked whether the assembly state of **K_SNEK$_S$** (unimer, nanoribbon, or nanohelix) might affect its ability to conduct ions in solution. As shown in Fig. 6, addition of 1 mg/mL unimeric APA **K_SNEK$_S$** to buffer (i.e., without allowing any time for self-assembly), regardless of salt concentration, did not increase the ionic conductivity of the solution (Buffer+unimers entries). Addition of 1 mg/mL assembled **K_SNEK$_S$** in 10 mM PB (nanoribbons) led to a small increase in conductivity over 10 mM buffer (increase of 0.4 x 10^2 μS/cm). However, addition of 1 mg/mL **K_SNEK$_S$** in 100 mM PB (nanohelices) led to a distinct increase in conductivity over 100 mM buffer alone (increase of 8.6 x 10^2 μS/cm). We also found that this increase in conductivity was much greater than addition of other charged polymers to 100 mM PB, all at 1 mg/mL (Table S4). These included poly(acrylic acid) (increase of 1.0 x 10^2 μS/cm), poly(sodium 4-styrene-sulfonate) (increase of 0.6 x 10^2 μS/cm), and alginic acid (increase of 0.7 x 10^2 μS/cm). The ability of **K_SNEK$_S$** nanohelices to increase conductivity was especially surprising considering that all three charged polymers have a greater number of charged species (carboxylates or sulfonates) per gram than the **K_SNEK$_S$** nanohelices. Finally, we also tested the ability of DNA to increase conductivity under the same conditions, measuring an increase of 1.7 x 10^2 μS/cm over 100 mM PB alone, which is 5-fold less than the **K_SNEK$_S$** nanohelices. We attribute the ion-carrying ability of **K_SNEK$_S$** to the close packing of the charged carboxylates in the nanohelices, which may enable rapid transport of sodium ions between the two electrodes in the conductivity meter; however, further experiments will need to be conducted to fully test this hypothesis.

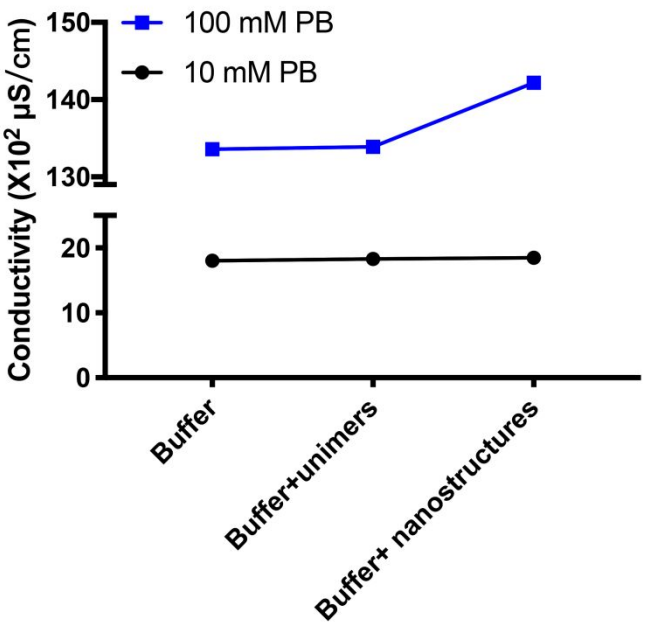

Fig. 6 Conductivity measurements of $\mathbf{K_SNEK_S}$ in monomeric state or assembled state at room temperature.

Proposed Mechanism of Nanohelix Formation

Our results suggest that both hydrophilic and hydrophobic interactions modulate the nanostructure morphology in these APAs. A possible mechanism for the formation of nanohelices at high PB concentrations as a consequence of charge screening is as follows: In general, the self-assembly pathway of these APAs proceeds *via* the formation of β-sheet tapes through hydrogen bonding at low buffer concentration (Figs. 2E and 2F black curves; Fig. S7). These β-sheet tapes have an intrinsic tendency to twist as a consequence of the constituent amino acid chirality, a propensity that is enhanced/impacted by electrostatic repulsions between like-charges. As revealed in the cryo-TEM images in Figs. 2A and 2B, $\mathbf{K_SNEK_S}$ and $\mathbf{K_S}\boldsymbol{C'}\mathbf{EK_S}$ nanoribbons possess bilayer molecular packing, which allows the glutamic acid residue in each APA to stabilize the nanostructures in PB. This molecular packing arrangement

would prevent nanoribbons from coiling up or aggregating due to repulsive forces among the negatively charged carboxylates on glutamic acid residues. Put succinctly, under low buffer concentration conditions, hydrophilic interactions dominate. Under high buffer concentration conditions, charge screening leads to a decrease in this repulsive force. With reduced repulsion between nearby glutamic acid residues in the nanoribbons, the nanoribbons then roll up to form the observed nanohelices. In the nanohelix morphology, the hydrophobic SATO components of the APAs pack more closely to minimize free energy and stabilize the nanostructure (hydrophobic interactions dominate). Meanwhile, the partially charged glutamic acid residues under high salt conditions continue to provide some amount of repulsion, stabilizing the nanostructures in the solution. Accordingly, the twisting of β-sheets within nanostructures becomes more homogeneous during the morphological transition, as indicated by the red shift in the amide I stretch in the FTIR spectra of both APAs (Fig. S7). In other words, in twisted nanoribbons, β-sheets near the center of the ribbons are more twisted than those at the periphery, while in nanohelices, β-sheets have a similar twist throughout the width of the ribbon (due to the cylindrical curvature); this phenomenon has been observed previously.[41] Thus, this delicate balance of forces that drive molecular packing allows persistent nanohelices to form, where the precise structure of the APA controls the distance between neighboring glutamic acid residues and ultimately the helical pitch. An illustrated depiction of the correlation among hydrophilic interactions, hydrophobic interactions, and the resultant self-assembled nanostructures is shown in Fig. 7.

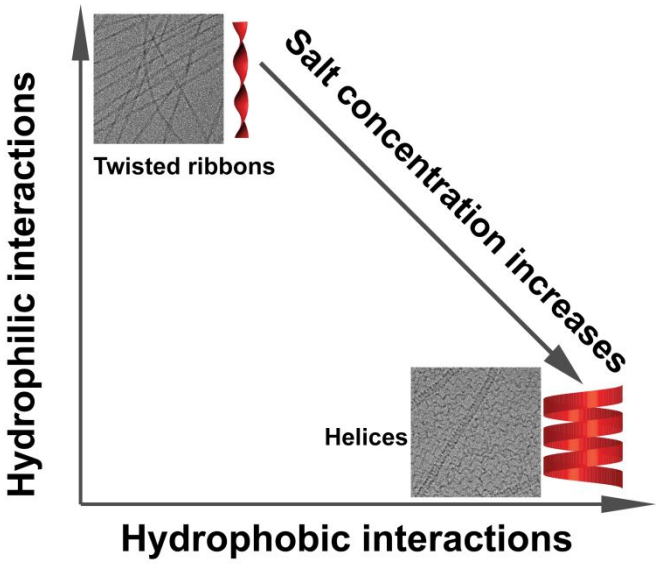

Fig. 7 Correlation among hydrophilic interactions, hydrophobic interactions, and the resultant self-assembled nanostructures.

Conclusions

In summary, we report here a simple strategy to induce formation of stable nanohelices from a series of APAs with the general structure $\mathbf{K_SXEK_S}$. Nanoribbons were observed at low concentrations of PB regardless of the X residue. Elevating the salt concentration facilitated formation of stable nanohelices due to suppressed repulsive interactions among glutamic acid residues. Coarse-grained molecular dynamics simulations of one APA, $\mathbf{K_SNEK_S}$, further revealed that hydrophilic interactions dominated the self-assembly process at low buffer concentration, leading to formation of nanoribbons, while hydrophobic interactions drove the formation of nanohelices at high buffer concentration. Interestingly, the nanohelices showed an marked increase in solution conductivity, while the nanoribbons did not, demonstrating the potential to use these nanohelices for charge transport. Overall, this work shows how subtle

changes in assembly conditions can be harnessed in short peptides to dictate different morphologies and new functions, potentially opening up a new field of ion-conducting, peptide-based materials.

Supporting information

Electronic supplementary information (ESI) available. See DOI:

Conflicts of interest

The authors declare no competing interests.

Acknowledgments

This work was supported by the National Science Foundation (DMR-1454754), the National Institutes of Health (R01GM123508) and the United States-Israel Binational Science Foundation (2016096), and also from start-up funds from Virginia Tech for S.A.D. We also thank the Dreyfus foundation for support of this work through a Camille Dreyfus Teacher-Scholar Award to J.B.M. We thank Prof. Michael Schulz (Virginia Tech) for DNA reagents, Prof. Tijana Grove (Virginia Tech) and her students for experimental assistance, Prof. Guoliang Liu and Dr. Tianyu Liu (Virginia Tech) for solution conductivity measurements, Einat Nativ-Rot from the electron microscopy unit at the Ilse Katz Institute for Nanoscale Science and Technology at BGU for cryo-TEM images, and Samantha J. Scannelli and Kearsley M. Dillon for careful readings of the manuscript. The authors also acknowledge use

of facilities within the Nanoscale Characterization and Fabrication Laboratory and the computational resources of Advanced Research Computing (ARC) at Virginia Tech. This research used resources of the National Energy Research Scientific Computing Center (NERSC), a U.S. Department of Energy Office of Science User Facility operated under Contract No. DE-AC02-05CH11231.

References

1. J. Howard and A. A. Hyman, Dynamics and mechanics of the microtubule plus end. *Nature*, 2003, **422**, 753-758.
2. H. Y. Kueh and T. J. Mitchison, Structural plasticity in actin and tubulin polymer dynamics. *Science*, 2009, **325**, 960-963.
3. T. Aida, E. W. Meijer and S. I. Stupp, Functional supramolecular polymers. *Science*, 2012, **335**, 813-817.
4. M. P. Hendricks, K. Sato, L. C. Palmer and S. I. Stupp, Supramolecular assembly of peptide amphiphiles. *Acc. Chem. Res.*, 2017, **50**, 2440-2448.
5. S. Fleming and R. V. Ulijn, Design of nanostructures based on aromatic peptide amphiphiles. *Chem. Soc. Rev.*, 2014, **43**, 8150-8177.
6. P. Worthington, S. Langhans and D. Pochan, Beta-hairpin peptide hydrogels for package delivery. *Adv. Drug Deliv. Rev.*, 2017, **110**, 127-136.
7. Y. Wang, A. G. Cheetham, G. Angacian, H. Su, L. S. Xie and H. G. Cui, Peptide-drug conjugates as effective prodrug strategies for targeted delivery. *Adv. Drug Delivery Rev.*, 2017, **110**, 112-126.
8. Y. Y. Lin, M. Penna, M. R. Thomas, J. P. Wojciechowski, V. Leonardo, Y. Wang, E. T. Pashuck, I. Yarovsky and M. M. Stevens, Residue-specific solvation-directed thermodynamic and kinetic control over peptide self-assembly with 1D/2D structure selection. *ACS Nano*, 2019, **13**, 1900-1909.
9. Q. G. Xing, J. X. Zhang, Y. Y. Xie, Y. F. Wang, W. Qi, H. J. Rao, R. X. Su and Z. M. He, Aromatic motifs dictate nanohelix handedness of tripeptides. *ACS Nano*, 2018, **12**, 12305-12314.
10. T. F. A. De Greef, M. M. J. Smulders, M. Wolffs, A. P. H. J. Schenning, R. P. Sijbesma and E. W. Meijer, Supramolecular polymerization. *Chem. Rev.*, 2009, **109**, 5687-5754.
11. H. A. M. Ardona, K. Besar, M. Togninalli, H. E. Katz and J. D. Tovar, Sequence-dependent mechanical, photophysical and electrical properties of pi-conjugated peptide hydrogelators. *J. Mater. Chem. C*, 2015, **3**, 6505-6514.
12. J. D. Tovar, R. C. Claussen and S. I. Stupp, Probing the interior of peptide amphiphile

supramolecular aggregates. *J. Am. Chem. Soc.*, 2005, **127**, 7337-7345.

13. D. Ivnitski, M. Amit, O. Silberbush, Y. Atsmon-Raz, J. Nanda, R. Cohen-Luria, Y. Miller, G. Ashkenasy and N. Ashkenasy, The strong influence of structure polymorphism on the conductivity of peptide fibrils. *Angew. Chem. Int. Ed.*, 2016, **55**, 9988-9992.
14. O. Silberbush, M. Engel, I. Sivron, S. Roy and N. Ashkenasy, Self-assembled peptide nanotube films with high proton conductivity. *J. Phys. Chem. B*, 2019, **123**, 9882-9888.
15. P. W. J. M. Frederix, I. Patmanidis and S. J. Marrink, Molecular simulations of self-assembling bio-inspired supramolecular systems and their connection to experiments. *Chem. Soc. Rev.*, 2018, **47**, 3470-3489.
16. O. S. Lee, S. I. Stupp and G. C. Schatz, Atomistic molecular dynamics simulations of peptide amphiphile self-assembly into cylindrical nanofibers. *J. Am. Chem. Soc.*, 2011, **133**, 3677-3683.
17. J. Nasica-Labouze, P. H. Nguyen, F. Sterpone, O. Berthoumieu, N. V. Buchete, S. Cote, A. De Simone, A. J. Doig, P. Faller, A. Garcia, A. Laio, M. S. Li, S. Melchionna, N. Mousseau, Y. G. Mu, A. Paravastu, S. Pasquali, D. J. Rosenman, B. Strodel, B. Tarus, J. H. Viles, T. Zhang, C. Y. Wang and P. Derreumaux, Amyloid β protein and Alzheimer's disease: When computer simulations complement experimental studies. *Chem. Rev.*, 2015, **115**, 3518-3563.
18. Y. Wang, K. Kaur, S. J. Scannelli, R. Bitton and J. B. Matson, Self-assembled nanostructures regulate H_2S release from constitutionally isomeric peptides. *J. Am. Chem. Soc.*, 2018, **140**, 14945-14951.
19. K. Lu, J. Jacob, P. Thiyagarajan, V. P. Conticello and D. G. Lynn, Exploiting amyloid fibril lamination for nanotube self-assembly. *J. Am. Chem. Soc.*, 2003, **125**, 6391-6393.
20. L. Ziserman, H. Y. Lee, S. R. Raghavan, A. Mor and D. Danino, Unraveling the mechanism of nanotube formation by chiral self-assembly of amphiphiles. *J. Am. Chem. Soc.*, 2011, **133**, 2511-2517.
21. L. Ziserman, A. Mor, D. Harries and D. Danino, Curvature instability in a chiral amphiphile self-assembly. *Phys. Rev. Lett.*, 2011, **106**, 238105.
22. D. Danino and E. H. Egelman, Direct imaging and computational cryo-electron microscopy of ribbons and nanotubes. *Curr. Opin. Colloid Interface Sci.*, 2018, **34**, 100-113.
23. J. Adamcik, V. Castelletto, S. Bolisetty, I. W. Hamley and R. Mezzenga, Direct observation of time-resolved polymorphic states in the self-assembly of end-capped heptapeptides. *Angew. Chem.-Int. Edit.*, 2011, **50**, 5495-5498.
24. T. Yamamoto, T. Fukushima, Y. Yamamoto, A. Kosaka, W. Jin, N. Ishii and T. Aida, Stabilization of a kinetically favored nanostructure: surface ROMP of self-assembled conductive nanocoils from a norbornene-appended hexa-peri-hexabenzocoronene. *J. Am. Chem. Soc.*, 2006, **128**, 14337-14340.
25. S. Zhong, H. G. Cui, Z. Y. Chen, K. L. Wooley and D. J. Pochan, Helix self-assembly through the coiling of cylindrical micelles. *Soft Matter*, 2008, **4**, 90-93.
26. Y. Wang, X. Z. Yang, T. Y. Liu, Z. Li, D. Leskauskas, G. L. Liu and J. B. Matson,

Molecular-level control over plasmonic properties in silver nanoparticle/self-assembling peptide hybrids. *J. Am. Chem. Soc.*, 2020, **142**, 9158-9162.

27. J. C. Foster, C. R. Powell, S. C. Radzinski and J. B. Matson, S-aroylthiooximes: a facile route to hydrogen sulfide releasing compounds with structure-dependent release kinetics. *Org. Lett.*, 2014, **16**, 1558-1561.
28. J. M. Carter, Y. Qian, J. C. Foster and J. B. Matson, Peptide-based hydrogen sulphide-releasing gels. *Chem. Commun.*, 2015, **51**, 13131-13134.
29. Y. Qian, K. Kaur, J. C. Foster and J. B. Matson, Supramolecular tuning of H_2S release from aromatic peptide amphiphile gels: Effect of core unit substituents. *Biomacromolecules*, 2019, **20**, 1077-1086.
30. A. Longchamp, K. Kaur, D. Macabrey, C. Dubuis, J. M. Corpataux, S. Deglise, J. B. Matson and F. Allagnat, Hydrogen sulfide-releasing peptide hydrogel limits the development of intimal hyperplasia in human vein segments. *Acta Biomater.*, 2019, **97**, 374-384.
31. H. G. Cui, A. G. Cheetham, E. T. Pashuck and S. I. Stupp, Amino acid sequence in constitutionally isomeric tetrapeptide amphiphiles dictates architecture of one-dimensional nanostructures. *J. Am. Chem. Soc.*, 2014, **136**, 12461-12468.
32. A. N. Moore and J. D. Hartgerink, Self-assembling multidomain peptide nanofibers for delivery of bioactive molecules and tissue regeneration. *Accounts Chem. Res.*, 2017, **50**, 714-722.
33. H. Rapaport, K. Kjaer, T. R. Jensen, L. Leiserowitz and D. A. Tirrell, Two-dimensional order in beta-sheet peptide monolayers. *J. Am. Chem. Soc.*, 2000, **122**, 12523-12529.
34. V. Castelletto, I. W. Hamley, C. Cenker and U. Olsson, Influence of salt on the self-assembly of two model amyloid heptapeptides. *J. Phys. Chem. B*, 2010, **114**, 8002-8008.
35. T. Otsuka, T. Maeda and A. Hotta, Effects of salt concentrations of the aqueous peptide-amphiphile solutions on the sol-gel Transitions, the gelation speed, and the gel characteristics. *J. Phys. Chem. B*, 2014, **118**, 11537-11545.
36. M. Konda, B. Kauffmann, D. B. Rasale and A. K. Das, Structural and morphological diversity of self-assembled synthetic gamma-amino acid containing peptides. *Org. Biomol. Chem.*, 2016, **14**, 4089-4102.
37. T. Otsuka and A. Hotta, Effects of salt concentrations on the structural transitions of peptide-amphiphile solution. *MRS Proceedings*, 2014, **1622**, 147-152.
38. J. F. Miravet, B. Escuder, M. D. Segarra-Maset, M. Tena-Solsona, I. W. Hamley, A. Dehsorkhi and V. Castelletto, Self-assembly of a peptide amphiphile: Transition from nanotape fibrils to micelles. *Soft Matter*, 2013, **9**, 3558-3564.
39. K. Kaur, Y. Wang and J. B. Matson, Linker-regulated H_2S release from aromatic peptide amphiphile hydrogels. *Biomacromolecules*, 2020, **21**, 1171-1178.
40. Y. Wang and J. B. Matson, Supramolecular nanostructures with tunable donor loading for controlled H_2S release. *ACS Appl. Bio Mater.*, 2019, **2**, 5093-5098.
41. E. T. Pashuck and S. I. Stupp, Direct observation of morphological tranformation from twisted ribbons into helical ribbons. *J. Am. Chem. Soc.*, 2010, **132**, 8819-8821.
42. S. J. Marrink, H. J. Risselada, S. Yefimov, D. P. Tieleman and A. H. de Vries, The

MARTINI force field: Coarse grained model for biomolecular simulations. *J. Phys. Chem. B*, 2007, **111**, 7812-7824.

43. S. A. Deshmukh, L. A. Solomon, G. Kamath, H. C. Fry and S. K. R. S. Sankaranarayanan, Water ordering controls the dynamic equilibrium of micelle-fibre formation in self-assembly of peptide amphiphiles. *Nat. Commun.*, 2016, **7**, 12367.
44. Z. Jiang, J. B. He, S. A. Deshmukh, P. Kanjanaboos, G. Kamath, Y. F. Wang, S. K. R. S. Sankaranarayanan, J. Wang, H. M. Jaeger and X. M. Lin, Subnanometre ligand-shell asymmetry leads to Janus-like nanoparticle membranes. *Nat. Mater.*, 2015, **14**, 912-918.
45. B. Smit, Phase-diagrams of Lennard-Jones fluids. *J. Chem. Phys.*, 1992, **96**, 8639-8640.
46. S. Mushnoori, K. Schmidt, V. Nanda and M. Dutt, Designing phenylalanine-based hybrid biological materials: controlling morphology via molecular composition. *Org. Biomol. Chem.*, 2018, **16**, 2499-2507.
47. O. S. Lee, V. Cho and G. C. Schatz, Modeling the self-assembly of peptide amphiphiles into fibers using coarse-grained molecular dynamics. *Nano Lett*, 2012, **12**, 4907-4913.
48. A. V. Sangwai and R. Sureshkumar, Coarse-grained molecular dynamics simulations of the sphere to rod transition in surfactant micelles. *Langmuir*, 2011, **27**, 6628-6638.
49. J. Feng, K. Y. Wong, G. C. Lynch, X. L. Gao and B. M. Pettitt, Salt effects on surface-tethered peptides in solution. *J. Phys. Chem. B*, 2009, **113**, 9472-9478.
50. I. Jelesarov, E. Durr, R. M. Thomas and H. R. Bosshard, Salt effects on hydrophobic interaction and charge screening in the folding of a negatively charged peptide to a coiled coil (leucine zipper). *Biochemistry-Us*, 1998, **37**, 7539-7550.
51. C. Goldhahn, J. Schubert, H. Schlaad, J. K. Ferri, A. Fery and M. Chanana, Synthesis of metal@protein@polymer nanoparticles with distinct interfacial and phase transfer behavior. *Chem. Mat.*, 2018, **30**, 6717-6727.
52. C. V. Kumar and A. Buranaprapuk, Tuning the selectivity of protein photocleavage: Spectroscopic and photochemical studies. *J. Am. Chem. Soc.*, 1999, **121**, 4262-4270.
53. M. P. Allen and D. J. Tildesley, *Computer simulation of liquids*, Clarendon Press; Oxford University Press, Oxford England New York, 1987.
54. R. Rabani, G. Heidarinejad, J. Harting and E. Shirani, Effect of wall stiffness, mass and potential interaction strength on heat transfer characteristics of nanoscale-confined gas. *Int. J. Heat Mass Transf.*, 2020, **147**, 118929.
55. M. M. Xu, L. X. Liu and Q. Yan, Allosterically activated protein self-assembly for the construction of helical microfilaments with tunable helicity. *Angew. Chem. Int. Ed.*, 2018, **57**, 5029-5032.
56. K. Kaur, Y. Qian, R. D. Gandour and J. B. Matson, Hydrolytic decomposition of *S*-aroylthiooximes: Effect of pH and *N*-arylidene substitution on reaction rate. *J. Org. Chem.*, 2018, **83**, 13363-13369.